The effect of operating conditions on the nitric oxide formation in anode baking furnace through numerical modeling

Nakate, Prajakta; Lahaye, Domenico; Vuik, Cornelis

Publication date
2021

Document Version
Final published version

Citation (APA)
Nakate, P., Lahaye, D., & Vuik, C. (2021). *The effect of operating conditions on the nitric oxide formation in anode baking furnace through numerical modeling*. (Reports of the Delft Institute of Applied Mathematics; Vol. 21-02). Delft University of Technology.

DELFT UNIVERSITY OF TECHNOLOGY

REPORT 21-02

The effect of operating conditions on the nitric oxide formation in anode baking furnace through numerical modeling

P.A. Nakate, D.J.P. Lahaye, C. Vuik

Reports of the Delft Institute of Applied Mathematics

Delft 2021

Article

The effect of operating conditions on the nitric oxide formation in anode baking furnace through numerical modeling

Prajakta Nakate [1,2], Domenico Lahaye [1,] and Cornelis Vuik [1,]

[1] Delft University of Technology; P.A.Nakate@tudelft.nl; D.J.P.Lahaye@tudelft.nl; C.Vuik@tudelft.nl
[2] Aluminium and Chemie, Rotterdam B.V.

Received: date; Accepted: date; Published: date

Abstract: Thermal nitric-oxide (NOx) formation in industrial furnaces due to local overheating is a widely known problem. Various industries made significant investments to reduce thermal NOx by varying the operating conditions and designs of the furnace. Finding optimal operating conditions or design parameters by experimenting in the furnace, however, is difficult. Numerical modeling can provide significant information in such cases. In this paper, a three dimensional steady state finite element model for the anode baking industrial furnace is discussed. The COMSOL Multiphysics software is used for modeling the non-premixed turbulent combustion and the conjugate heat transfer to the insulation lining. The mesh generation using the cfMesh software allows to increase the spatial resolution locally at the outlet of the fuel nozzles while maintaining the overall quality of the mesh. The temperature and species mass fraction obtained from the finite element model are calibrated by adjusting the amount of artificial diffusion in the transport equations for the species. The simulated temperature agrees well with the measured data from our industrial partner in regions distant from the flames. The model underestimates the measured oxygen mass fraction. The spatial gradients in oxygen mass fraction, however, are captured well by the model. The effects of variation of the fuel mass flow rate and the fuel pipe diameter on the NOx generation are studied. The results show that by decreasing the fuel mass flow rate and increasing the fuel pipe diameter by 45%, the peak in thermal NOx ppm generated in the furnace decreases by 42%.

Keywords: Thermal NOx formation; Industrial furnace; Diffusion tuning; Eddy dissipation model; P1 approximation model

1. Introduction

Industrial emissions are discussed worldwide due to its significant impact on climate change. Among the various hazardous gases emitted, reducing nitrogen oxides have been a priority for many industries. These nitrogen oxides are often referred to as NOx. The NOx formation can be attributed to four prime processes. The thermal NOx, which is the largest contributor, is formed from the atmospheric nitrogen at the temperatures higher than 1300^0C. The other three processes are prompt NOx, fuel NOx formed by the nitrogen containing fuels and NOx formation in lean mixtures at elevated pressures via intermediate formation of N_2O [1]. The study of high temperature regions is required since the majority of NOx formation in industries is by thermal process. Studying these temperatures by a traditional trial and error approach is difficult. These methods can also lead to longer times and may require higher resources. Moreover, sometimes dealing with high temperatures in the furnace for the experiment is impossible. Therefore, learning from the numerical model of these processes is preferred.

NOx emissions from industrial furnaces have been widely discussed [2]. Anode baking process is one example in which the thermal NOx is formed due to high temperatures. The heat required for the baking process is produced by the combustion of natural gas in a furnace. The resulting temperature in the furnace is well above 1300^0C. Therefore, the thermal NOx produced in the furnace is significant. In

Table 1. List of symbols

Nomenclature			
Symbol	**Meaning**	**Symbol**	**Meaning**
ρ	Density, kg/m^3	h	Mesh size, m
$\mathbf{u}$	Velocity, m/s	β	Convective velocity vector, m/s
p	Reference press, Pa	ν	Stochiometric coefficient
μ	Dynamics viscosity, $kg/m/s$	τ_T	Turbulent time scale, s
μ_T	Turbulent viscosity, $kg/m/s$	C_p	Specific heat capacity, $J/kg/^oC$
$\mathbf{k}$	Turbulent kinetic energy, m^2/s^2	T	Temperature, ^oC
ϵ	Turbulent dissipation rate, m^2/s^3	q	Heat flux, $J/m^2/s$
I_T	Turbulent intensity, %	Q	Heat source, J/m^3
L_T	Turbulent length scale, m	k	Thermal conductivity, $W/m/^oC$
w	Mass fraction	Q_r	Radiative heat source, J/m^3
D^f	Fick's diffusion coefficient, m^2/s	κ	Absorption coefficient, $1/m$
M_n	Mean molar mass, kg/mol	I_b	Black body radiation, W/m^2
c_{art}	Artificial diffusion coefficient, m^2/s	G	Incident radiation, W/m^2
δ_{id}	Tuning parameter	ξ	Emissivity
Subscripts			
i	Chemical species	p	Product
r	Reactant	ED	Eddy dissipation
MV	Mean value	$fluid$	Fluid domain
$solid$	Solid domain	$P1$	P1 approximation model
Superscripts			
for	Forward	rev	Reverse

this work, the anode baking furnace of the company named Aluchemie in Rotterdam, Netherlands is studied to reduce the NOx from the furnace. The various physics involved in the process are turbulent flow, combustion, radiation and conjugate heat transfer. The multi-physics modeling can be carried out to analyse the temperature in the furnace. This can provide significant information on the generation of NOx. The anode baking process practiced in Aluchemie furnace is described in the previous paper [13] that describes the aerodynamics in the furnace. The study on NOx emissions continues in this paper. Therefore, as detailed in the previous paper, the heating section of the furnace is important for the study of NOx formation.

The modeling of the anode baking process is used since 1980's. The earlier developed models lacked the complexity due to limited resources and knowledge [3]. However, they provide strong foundation to the models developed in the later stage. The modeling of anode baking process improved significantly in the last few decades starting from 2D models to more sophisticated 3D models. The focus of the modeling has been on the optimized furnace design, increasing the energy efficiency and decreasing the wall deformation [4–9]. Moreover, there have been studies to propose comparisons between various models for the turbulent flow, combustion and radiation [10,11]. These models help to establish the state-of-the-art models. The NOx formation in the anode baking furnace started gaining interest since last few years. The recent models developed by Tajik et.al. [12] examines the effect of inlet oxygen concentration, inlet oxygen temperature, equivalence ratio and thermal properties of refractory walls on the NOx formation. The study suggests a significant impact on NOx by changing inlet oxygen concentration and temperature. The thermal NOx formation highly depends on the maximum temperature in the furnace. The temperature depends on the other operating conditions related to the fuel inlet that governs the mixing phenomena of the two streams. Studying the mixing behaviour of the two streams with respect to the NOx formation are still lacking.

The aim of this paper is to provide insights on the NOx formation with respect to the operating conditions such as fuel mass flow rate and fuel pipe diameter. The variations in these operating conditions result in different flow dynamics in the furnace. The change in the flow dynamics affects

the mixing patterns of the fuel and air streams. To study the effect of these operating conditions, a 3D steady state model is developed using COMSOL Multiphysics software. The turbulent flow is modeled by the RANS equation. The Reynolds stresses are closed by using the standard k-ϵ model. The combustion and radiation are modeled using eddy dissipation and P1 approximation model. To model the heat flux conducted to the solid domain, a brick layer is added to the model. The temperatures measured in the furnace are provided as boundary condition at the brick layer not in contact with the gas domain. The NOx is computed in the post processing stage using a Zeldovich mechanism. In the first part of the paper, the test case model of the existing fuel mass flow rate and fuel pipe diameter is studied. The tuning of the diffusion parameter is carried out by comparing with measured values. The requirement of tuning diffusion in the model equation is discussed. The effect of fuel mass flow rate and fuel pipe diameter on NOx generation are studied. The higher mass flow rate results in higher turbulent viscosity ratio that further increases the NOx formation due to higher temperature in the furnace. Furthermore, the effect of the increasing fuel pipe diameter decreases the turbulent scale thereby lowering the temperature. Therefore, increasing the fuel pipe diameter decreases the NOx in the furnace.

2. Geometry and mesh

The NOx generation in the anode baking furnace occurs in the heating section. In this study, the focus is on modeling the NOx generated in the anode baking furnace. This allows us to restrict to a heating section of the furnace for the model geometry. In order to account for the heat flux going to the anodes, a brick layer is added along the flue domain as shown in Figure 1. Aluchemie has measured the temperatures at the brick sides using several thermocouples. As the focus in this study is on NOx generation, the interest lies in the temperature distribution in the flue domain. By taking the boundary conditions as the measured temperatures on the brick layer, the heat flux leaving the flue domain can be modeled accurately. Therefore, the model is simplified and restricted to a flue gas domain and the solid brick layer. The approximate dimensions in the XY plane are as shown in Figure 1. The symmetry is assumed at the flue domain side to reduce the computational time. The dimensions of the model comply with the Aluchemie furnace. The depth of the fluid domain and the brick layer domain in the Z direction are 0.27 m and 0.11 m, respectively. The details of the internal geometry of the fluid domain is elaborated in our previous paper [13] in which the aerodynamics in the flue domain of the furnace is studied. As shown in the figure, the air enters the fluid domain from three inlets whereas there are two fuel inlets at the top. The air and fuel streams are mixed in a cross flow manner.

Aluchemie has measured NOx emissions by varying the nozzle diameters of the burners. In this paper, the burner is simplified to a simple pipe with length 0.11 m. The two diameter values 9 mm and 13 mm of the pipes are considered based on the nozzle diameters of the actual burners. The remaining geometry of the model for the two studies remains the same.

The meshing of the geometries with two diameters of the fuel pipes are carried out with the cfMesh software. In our previous paper, the analysis of different meshing techniques are discussed [13]. The less diffusive Cartesian mesh for the complex geometry of the anode baking furnace can be obtained using cfMesh software. The region under the fuel outlet is refined further for better resolution of the flow in that region. This region is particularly of interest with respect to NOx generation. Figure 2 shows the meshes of the geometries with the two diameters. It can be observed that the region of the jet development is refined in the same manner for both geometries. The difference is only with respect to the diameter of the fuel pipe. Table 2 provides the details of the two meshes.

Table 2. Details of the meshes of two geometries with different fuel pipe diameter

Diameter of fuel pipe [mm]	Number of elements	Size of elements in refinement zone [mm]	Quality of mesh
9	892784	3	0.89
13	1352854	3	0.84

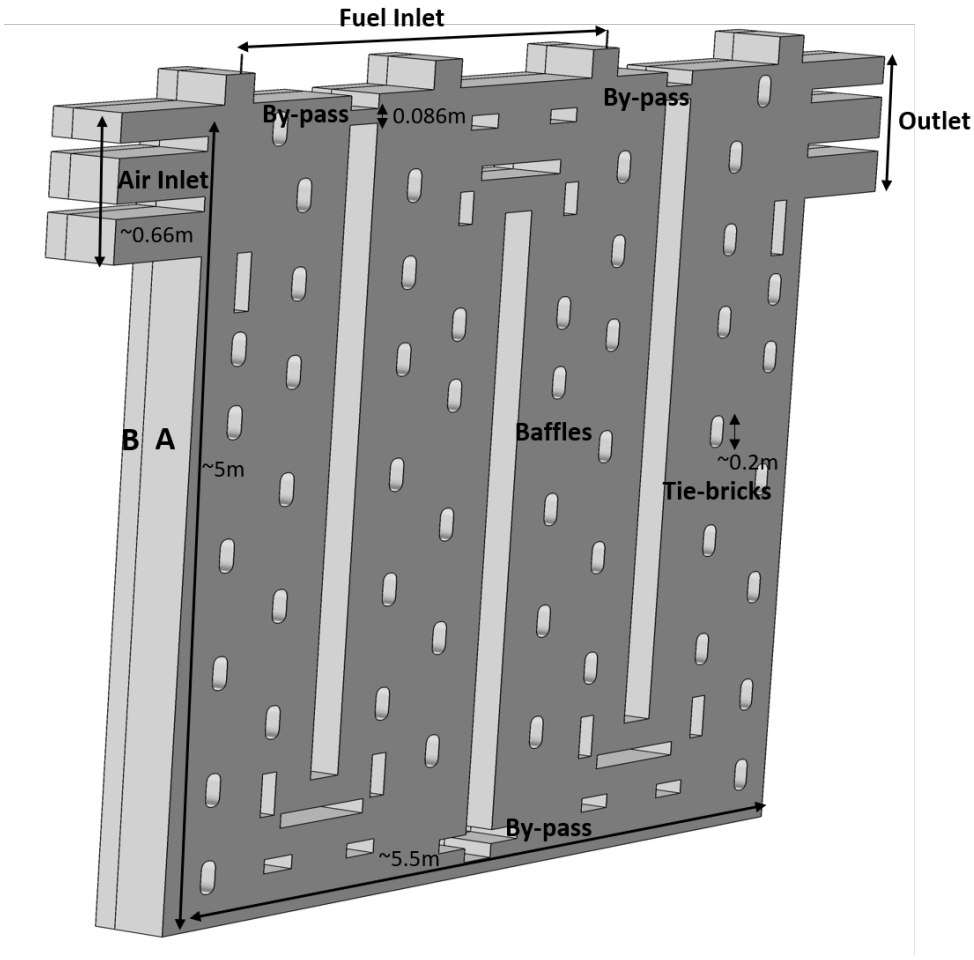

Figure 1. The 3D geometry of the heating section of anode baking furnace with fluid and solid domain. Domain A is the fluid domain with gaseous interactions and domain B is the refractory brick layer.

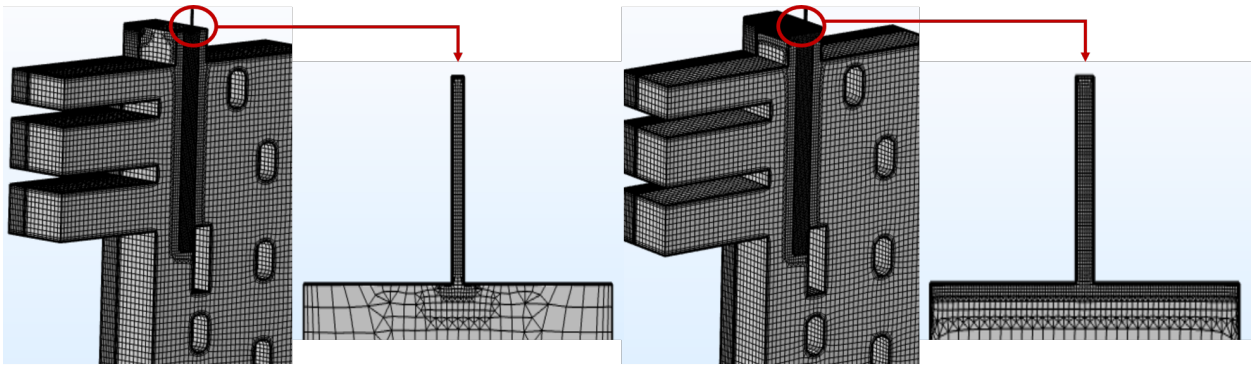

Figure 2. Comparison of the meshes of geometries with fuel pipe diameters (a) 9 mm and (b) 13 mm. Two meshes of two models differ only at the attachment of fuel pipe to the furnace.

The quality of the mesh is measured by the skewness parameter. Obtaining a mesh of similar mesh quality for two diameter of fuel pipes is difficult with the default mesher of COMSOL Multiphysics. Figure 3 shows the mesh quality histograms in terms of skewness for different diameters of fuel pipe. It can be observed that in some regions of the 13 mm diameter of fuel pipe there are more elements that are of low quality as compared to the 9 mm diameter. However, the overall histogram quality is

comparable. cfMesh software provides control over the size of elements in the region of interest and therefore, obtaining meshes with the external software is preferred.

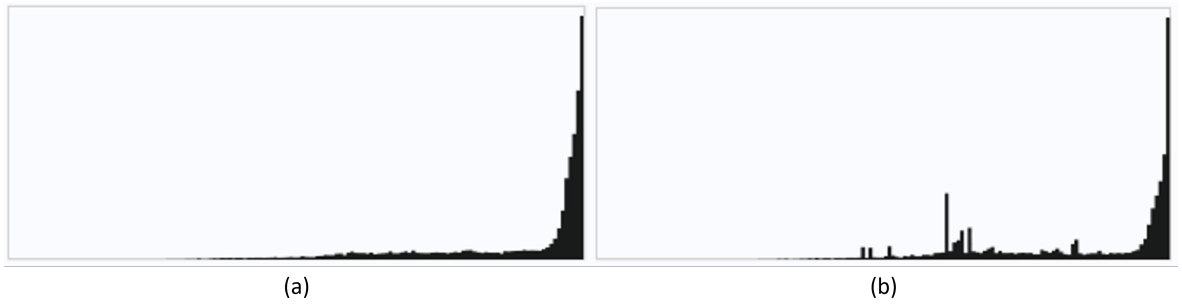

Figure 3. Histogram of the skewness of the cell in the mesh for the geometry with fuel pipe diameter equal to (a) 9mm and (b) 13mm. Meshes of comparable quality can be obtained using the cfMesh software.

3. Model equations

3.1. Turbulent flow model

The turbulent flow is modeled using Reynolds average Navier-Stokes (RANS) equation as presented in Equation (1).

$$\rho(\mathbf{u}\cdot\nabla)\mathbf{u} = \nabla\cdot[-p\mathbf{I}+\mathbf{K}], \tag{1}$$

The term **K** is defined by Equation (2).

$$\mathbf{K} = (\mu+\mu_t)(\nabla\mathbf{u}+(\nabla\mathbf{u})^T) - \frac{2}{3}(\mu+\mu_t)(\nabla\cdot\mathbf{u})\mathbf{I} - \frac{2}{3}\rho k\mathbf{I}, \tag{2}$$

The standard $k-\epsilon$ model is used for closing the Reynolds stresses from the RANS equation. The model is the two equation turbulent model defined by the transport equation of turbulent kinetic energy and turbulent dissipation rate as shown in Equation (3) and (4), respectively.

$$\rho(\mathbf{u}\cdot\nabla)k = \nabla\cdot[(\mu+\frac{\mu_t}{\sigma_k})\nabla k] + P_k - \rho\epsilon \tag{3}$$

$$\rho(\mathbf{u}\cdot\nabla)\epsilon = \nabla\cdot[(\mu+\frac{\mu_t}{\sigma_\epsilon})\nabla\epsilon] + C_{\epsilon1}\frac{\epsilon}{k}P_k - C_{\epsilon2}\rho\frac{\epsilon^2}{k}. \tag{4}$$

The production term P_k is as presented in Equation (5).

$$P_k = \mu_T(\nabla\mathbf{u}:(\nabla\mathbf{u}+(\nabla\mathbf{u})^T) - \frac{2}{3}(\nabla\cdot\mathbf{u})^2) - \frac{2}{3}\rho k\nabla\cdot\mathbf{u} \tag{5}$$

The definition of turbulent viscosity μ_T with the standard $k-\epsilon$ model is given in Equation (6).

$$\mu_T = \rho C_\mu\frac{k^2}{\epsilon} \tag{6}$$

The values of the constant parameters for the Equations (3) and (4) are given in Table 3.

The boundary conditions for the turbulent kinetic energy and turbulent dissipation rate are defined in terms of turbulent length scale and turbulent intensity. These definitions are as presented in Equation (7) and (8), respectively.

$$k = \frac{3}{2}(U_{ref}I_T)^2 \tag{7}$$

Table 3. Values of the constants for standard k-ϵ model.

Constant	Value
C_μ	0.09
$C_{\epsilon 1}$	1.44
$C_{\epsilon 2}$	1.92
σ_k	1.00
σ_ϵ	1.30

$$\epsilon = C_\mu^{(3/4)} \frac{k^{(3/2)}}{L_T}. \tag{8}$$

3.2. Eddy dissipation combustion model

Methane is used as fuel in the anode baking process. A simplified one step combustion mechanism of methane is used to quantify chemical species. The reaction is as follows.

$CH_4 + 2\,O_2 \longrightarrow CO_2 + 2\,H_2O$

The transport equation for each of the species is given by Equation (9) and (10).

$$\nabla \cdot \mathbf{j}_i + \rho(\mathbf{u} \cdot \nabla) w_i = R_i \tag{9}$$

$$\mathbf{j}_i = -(\rho D_i^f \nabla w_i + \rho w_i D_i^f \frac{\nabla M_n}{M_n}) \tag{10}$$

The isotropic diffusion can be added to the diffusion coefficient from Equation (10). This additional diffusion can be varied using a tuning parameter δ_{id} from Equation (11). In a later section, the effect of variation of this tuning parameter is studied.

$$c_{\text{art}} = \delta_{\text{id}} h ||\beta|| \tag{11}$$

The reaction term from Equation (9) is modeled using the eddy dissipation model.The regularization is implemented to ensure that the reactant is consumed only when its mass fraction value is higher than zero. Moreover, the mass fraction of the product is restricted to take the maximum value of 1. The eddy dissipation model equations are given by Equation (12) to (16).

$$R_i = \frac{1}{2} \frac{R_i^c - |R_i^c|}{\max(w_i, w_i^{dl})} \max(w_i, 0) + \frac{1}{2} \frac{R_i^c + |R_i^c|}{\max(1 - w_i, w_i^{dl})} \max(1 - w_i, 0) \tag{12}$$

$$R_i^c = \nu_i M_i [\min(r_{MV,i}^{for}, r_{ED,i}^{for}) - \min(r_{MV,i}^{rev}, r_{ED,i}^{rev})] \tag{13}$$

$$r_{MV,i}^{for} = k^{for} \prod_r (\frac{\rho w_r}{M_r})^{-\nu_{i,r}}, \qquad r_{MV,i}^{rev} = k^{rev} \prod_p (\frac{\rho w_p}{M_p})^{-\nu_{i,p}} \tag{14}$$

$$r_{ED,i}^{for} = \frac{\alpha\epsilon}{k} \rho \min[\min(\frac{w_r}{\nu_r M_r}), \beta \sum_p (\frac{w_p}{\nu_p M_p})] \tag{15}$$

$$r_{ED,i}^{rev} = \frac{\alpha\epsilon}{k} \rho \min[\min(\frac{w_p}{\nu_p M_p}), \beta \sum_r (\frac{w_r}{\nu_r M_r})] \tag{16}$$

The default values of α=4 and β=0.5 are used. The turbulent time scale determines the mixing intensity of the fuel and oxidizer streams. The Dirichlet boundary conditions are specified for all chemical species transport equations.

3.3. Energy equation coupled with Radiation and conjugate heat transfer

The energy transport equation for the gas domain in which the combustion process of methane occurs is presented by Equation (17). The specific heat capacity of gases, namely, CH_4, O_2, CO_2, H_2O and, N_2 are defined by a temperature dependent analytical function. The parameters specific to a certain gas are obtained from NIST database. The specific heat capacity for the mixture of gases is then calculated considering the contribution of each of the gas.

$$\rho C_p \mathbf{u} \cdot \nabla T + \nabla \cdot \mathbf{q} = Q \tag{17}$$

The combustion of methane translates into the generation of heat energy. This acts as a heat source term, Q, in the energy transport equation solved for the gas domain. The heat energy generated from the combustion process is computed based on the heat of the formation of each of the chemical species and the stoichiometric coefficient of the single step combustion of methane. The heat flux, q, is given by Fourier's law as given in Equation (19).

$$\mathbf{q} = -k_{fluid} \nabla T \tag{18}$$

The heat generated in the gas domain is conducted through walls to anodes. In this model, a single brick layer is considered so as to account for the heat flux conducting to a combined solid phase.

$$\mathbf{q} = -k_{solid} \nabla T \tag{19}$$

The radiation in the gas domain is accounted by the radiative source term as presented in Equation (20). The incident radiation, G, is computed by the P1 approximation model as defined by the Equation (21).

$$Q_r = \kappa(G - 4\pi I_b) \tag{20}$$

$$\nabla \cdot (D_{P1} \nabla G) - \kappa(G - 4\pi I_b) \tag{21}$$

The diffusion coefficient of the P1 approximation is defined based on the absorption and scattering coefficient as presented in Equation (22). The scattering is neglected by assigning value zero to σ_s.

$$D_{P1} = \frac{1}{3(\kappa + \sigma_s)} \tag{22}$$

The radiative flux through boundaries is defined by Equations (23) and (24). The emissivity of the walls is defined by the temperature dependent interpolation function based on the data provided by the brick manufacturer.

$$-\mathbf{n} \cdot (-D_{P1} \nabla G) = -q_{r,net} \tag{23}$$

$$q_{r,net} = \frac{\xi}{2(2 - \xi)} (4\pi I_{b,w}(T) - G) \tag{24}$$

3.4. NOx calculations by Zeldovich mechanism

The NOx is calculated in the post processing stage by solving stabilized convection diffusion equation as given by Equation (25).

$$\nabla \cdot (\rho \mathbf{u} w_{\mathrm{NO}}) = \nabla \cdot (\rho D^f \nabla w_{\mathrm{NO}}) + S_{\mathrm{NO}} \tag{25}$$

The thermal NOx source term from Equation (25) is modeled in the post processing stage using the extended Zeldovich mechanism. Following two major reactions govern the formation of thermal NOx.

$O + N_2 \rightleftharpoons N + NO$

$N + O_2 \rightleftharpoons O + NO$

Whereas, the third reaction is significant only in the fuel rich mixtures.

$N + OH \rightleftharpoons H + NO$

The rate constants for these reactions are provided in Table 4.

Table 4. Rate constants of the Zeldovich mechanism reactions

Rate constant	Value [m^3/mol-s]
$k_{f,1}$	$1.8\times10^{8}e^{-38370/T}$
$k_{f,2}$	$1.8\times10^{4}Te^{-4680/T}$
$k_{f,3}$	$7.1\times10^{7}e^{-450/T}$
$k_{r,1}$	$3.8\times10^{7}e^{-425/T}$
$k_{r,2}$	$3.81\times10^{3}Te^{-20820/T}$
$k_{r,3}$	$1.7\times10^{8}e^{-24560/T}$

The net rate of formation of NO based on the listed reactions and quasi-steady state assumption for the concentration of N radical is given by Equation (26).

$$\frac{d[NO]}{dt} = 2k_{f,1}[O][N_2]\frac{(1-\frac{k_{r,1}k_{r,2}[NO]^2}{k_{f,1}[N_2]k_{f,2}[O_2]})}{(1+\frac{k_{r,1}[NO]}{k_{f,2}[O_2]+k_{f,3}[OH]})} \tag{26}$$

The O radical concentration is calculated based on the equilibrium approach and is given by Equation (27).

$$[O] = 3.97\times10^{5}T^{-1/2}[O_2]^{1/2}e^{-31090/T} \tag{27}$$

The source term from Equation (25) is calculated using Equation (28).

$$S_{NO} = M_{NO}\frac{d[NO]}{dt} \tag{28}$$

3.5. Finite element discretization and solver

In this paper, COMSOL Multiphysics software version 5.4 is used for the numerical modeling of the furnace. The software is based on the finite element discretization of the transport equations [14]. The details of the discretization as well as the solver settings for the turbulent flow are described [13]. A linear type of elements are considered for discretizing all transport equations of chemical species as well as radiative transport equation using the finite element method.

The model consists of several physics. In such problems, solving all variables in a single iteration leads to huge memory requirements. The segregated solver in such cases improves the performance significantly. Therefore, a segregated solver approach by defining different segregated steps for relevant groups of variables is used to simulate the model. The segregated solver approach is explained in detail in the previous paper [13]. Table 5 shows the segregated groups that the solver encounters while solving the model. For all segregated groups, the Newton-Raphson method with a constant damping factor is applied to linearize the non-linear transport equation. The Jacobian for the Newton method is updated after every iteration. The corresponding direct/iterative solver for solving the linear equation for each of the segregated step is also mentioned in Table 5.

4. Results and discussion

In this paper, the effect of various operating conditions related to the mixing behaviour of air and fuel stream are studied. In the first part of this section the results of test case are discussed. The test case is defined by the existing burner design and the operating conditions with the commonly used diffusion parameter settings of the model. In the subsequent parts, the effect of tuning of diffusion

Table 5. Details of the segregated solver for individual physics

Segregated step	Variables	Linear solver	Preconditioner
Segregated step 1	u, p	GMRES iterative solver	Algebraic multigrid preconditioner
Segregated step 2	T	Pardiso direct solver	-
Segregated step 3	k, ϵ	GMRES iterative solver	Algebraic multigrid preconditioner
Segregated step 4	w_i	GMRES iterative solver	Algebraic multigrid preconditioner
Segregated step 5	G	Pardiso direct solver	-

parameter, effect of increasing the velocity of fuel stream and the effect of increasing the fuel pipe diameter are discussed. The following table (Table 6) provides the summary of all models examined in this section. Note that for all models, the air stream remains unchanged at 0.18 kg/s.

Table 6. Summary of models discussed in this paper

Description	Diffusion tuning parameter	Fuel jet velocity	Fuel pipe diameter
Test case	0	74 m/s	9 mm
Effect of diffusion	0, 0.1, 0.3 & 0.5	74 m/s	9 mm
Effect of fuel jet velocity	0.1	50, 74 & 90 m/s	9 mm
		24 35 & 43 m/s	13 mm
Effect of fuel pipe diameter	0.1	74 m/s	9 mm
		35 m/s	13 mm

The velocity for the 13 mm diameter fuel pipe model are decided based on the equivalent fuel mass flow rate from 9 mm diameter. Table 7 shows the values of velocities for the two fuel pipe diameters that yields equal mass flow rate of fuel injected in the furnace. As can be expected, for the larger diameter of fuel pipe, the injected fuel inlet velocity is lower.

Table 7. Values of fuel pipe diameters and velocities that have equivalent mass flow rate

Fuel mass flow rate [kg/s]	Fuel pipe diameter [mm]	Fuel inlet velocity [m/s]
0.0020	9	50
	13	24
0.0030	9	74
	13	35
0.0037	9	90
	13	43

4.1. Results of the test case model

In this section, the results of the test case model are discussed. The test case model is with 9 mm fuel pipe diameter and fuel mass flow rate of 0.003 kg/s. The test case model is the representation existing design from the Aluchemie. The results are compared with the measured values from the furnace. It is important to understand the formation of NOx with the existing design. Further analysis to reduce the NOx from the furnace can be extended based on the validated model for the existing design.

The model of the 9 mm pipe diameter is developed systematically in this study. The detailed analysis of the non-isothermal turbulent flow modeling with different meshing techniques is carried out in our previous paper [13]. The results with cfMesh software with the refinement under the fuel outlet provides more accurate results. This model is further improved by adding transport of chemical species, radiation and conjugate heat transfer. In this section, the results of the 9 mm fuel pipe diameter are explained.

Figure 4 shows the velocity distribution in the furnace. The inlet velocity for the 9 mm diameter of fuel pipe is 74 m/s. It can be observed that the velocity at the outlet of the fuel pipe is as high as 120 m/s. The high momentum of the jet is responsible for the deeper penetration of jet in the furnace. The velocity of the jet is such that the combustion gases does not flow through the bypass at the top. The higher momentum ensures that the combustion is well distributed in the furnace as explained later.

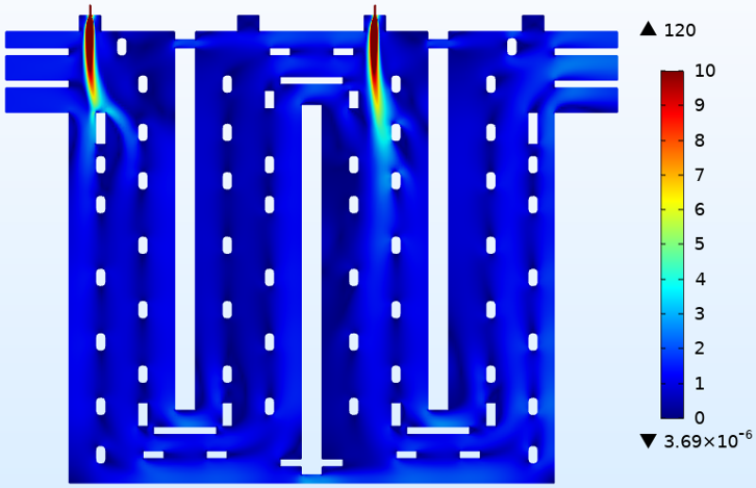

Figure 4. Velocity magnitude distribution [m/s] in the furnace with 9 mm fuel pipe diameter for fuel mass flow rate of 0.003 kg/s. The momentum of the jet is such that fuel stream is penetrated well within the furnace.

After developing the initial flow results, the transport of chemical species is included in the model. The turbulent chemistry interaction is modeled by the eddy dissipation model. This model is based on the 'mixed is burnt' phenomena. This can be observed from the mass fraction distribution of CH_4 (reactant) and mass fraction distribution of CO_2 (product) as shown in Figure 5 and 6, respectively. The layer of CH_4 stream that is in contact with the O_2 shows the appearance of the product (CO_2). The reaction zone is limited to the mixing zone of the reactants. This produces sharp gradients of the chemical species throughout the model of the furnace. This result can be attributed to the source term calculated by the eddy dissipation model. The source term of the reaction in eddy dissipation model is strongly related to the turbulence parameters that govern mixing.

Due to the larger penetration of the jet associated with the high momentum, the combustion reaction zone is not limited to the region near the fuel outlet. Moreover, Figure 5 shows that as compared to the first burner, the traces of CH_4 remain longer in the flame for the second burner. The combustion in the section of the furnace is an example of two staged combustion. Therefore, the air/fuel ratio for the second burner is reduced as compared to the first burner. The stream after the second stage of combustion consists of products from the first stage as well. This causes delayed mixing of the fuel with the oxidizer leaving traces of fuel for longer stream. Moreover, the concentration of CO_2 is higher downstream the second burner. This is the result of mixing of CO_2 formed by the second burner fuel with that of CO_2 formed due to the reaction of fuel from first burner and oxidizer. The overall results provided by the eddy dissipation model follows a streamline and the diffusion is found to be negligible.

The heat energy released by the combustion reaction is modeled using the enthalpy of reaction. The enthalpy of reaction is further calculated based on the stoichimetric coefficient and the enthalpy of formation for the individual species in the reaction. The heat transfer equation is updated by adding the source term of heat of combustion reaction. Figure 7 shows the temperature distribution in the furnace by adding this source term. It can be observed that the high temperature region in the furnace is coinciding with the combustion reaction zone. Therefore, the temperature follows the streamline where the CO_2 is higher. It can be observed that the central part of the jet is colder than the outer part.

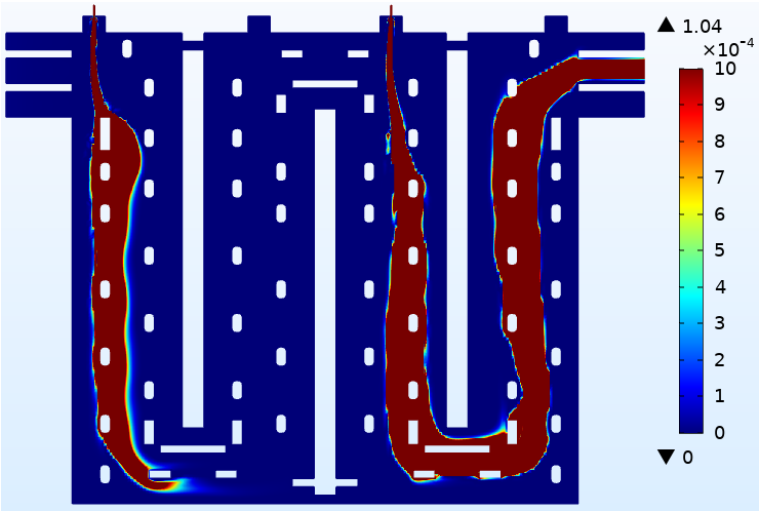

Figure 5. Mass fraction distribution of CH_4 in the furnace with 9 mm fuel pipe diameter and 0.003 kg/s fuel mass flow rate. The two staged combustion can be observed with incomplete burning of the fuel.

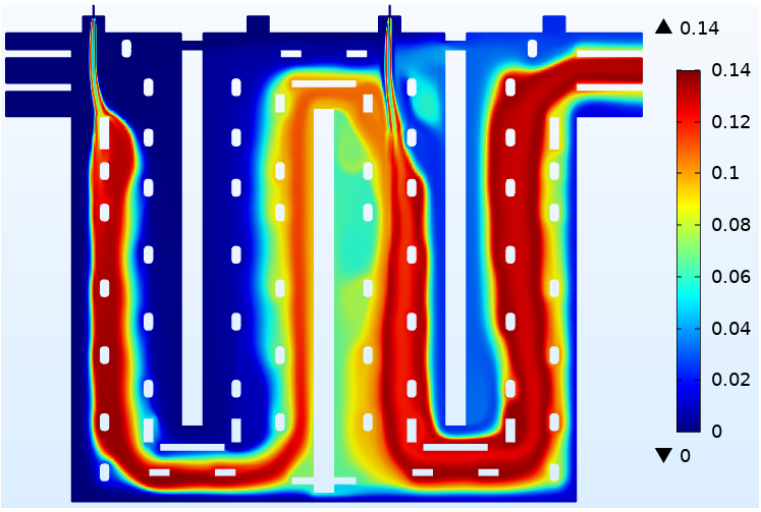

Figure 6. Mass fraction distribution of CO_2 in the furnace with 9 mm fuel pipe diameter and 0.003 kg/s fuel mass flow rate. The reaction zone is restricted to a narrow stream at both stages.

This can be attributed to the high momentum of the jet. Due to the momentum, the fuel does not mix with the oxidizer completely. This results in the combustion reaction occurring only at the outside layer. Therefore, the outer part is hotter compared to the central layer of the flame.

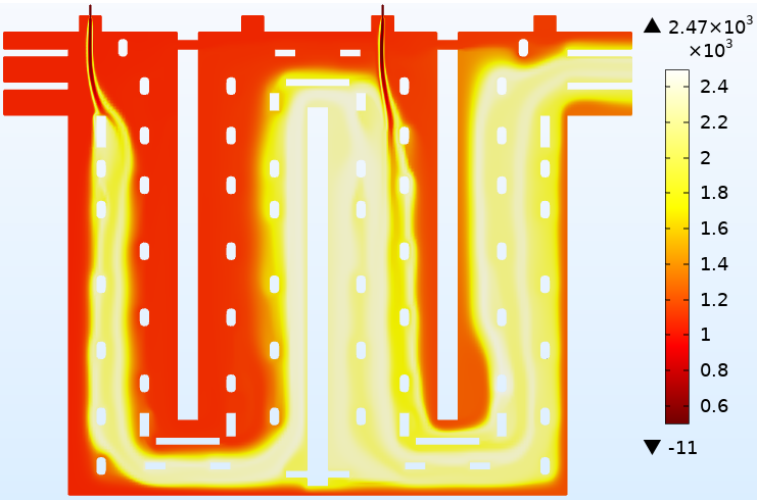

Figure 7. Temperature distribution [^{o}C] of in the furnace with 9 mm fuel pipe diameter and 0.003 kg/s fuel mass flow rate without considering the radiation. The narrow streamed higher temperatures zones follow from the reaction zones. Temperature at outlet side is higher compared to after the first stage burning.

The maximum temperature in the furnace is as high as 2470 ^{0}C in case of no radiative heat transfer. Moreover, the lower temperature calculated by the model is unrealistic and as low as -11 ^{0}C. Therefore, heat transfer by radiation is important phenomena in the anode baking furnace that needs to be incorporated in the modeling. The radiation is modeled by the P1 approximation model. As can be observed from Figure 8, the temperature distribution becomes more uniform by accounting radiation. The maximum temperature is lowered to 2225 ^{0}C due to the heat transfer. The high temperature region is restricted to a layer of combustion reaction zone in the jet.

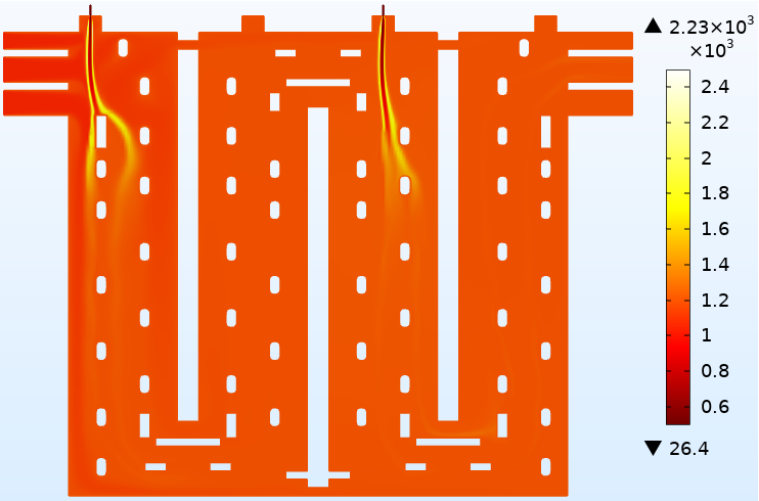

Figure 8. Temperature distribution [^{o}C] of in the furnace with 9 mm fuel pipe diameter and 0.003 kg/s fuel mass flow rate by considering the radiation. The temperature distribution improves by the addition of radiation along with decreasing the maximum temperature.

Another important physical phenomena in the anode baking furnace is the transfer of heat to the anodes. In order to consider the heat flux leaving the gas domain a single brick layer is considered in the model. The temperature measured at the Aluchemie furnace at the brick. Figure 9 shows the transfer of heat from the fluid domain at the plane passing through both burners.

The temperature calculated from the model is compared against the measured temperature from the furnace. The measurement in the furnace is carried out using an IR thermographic camera (details

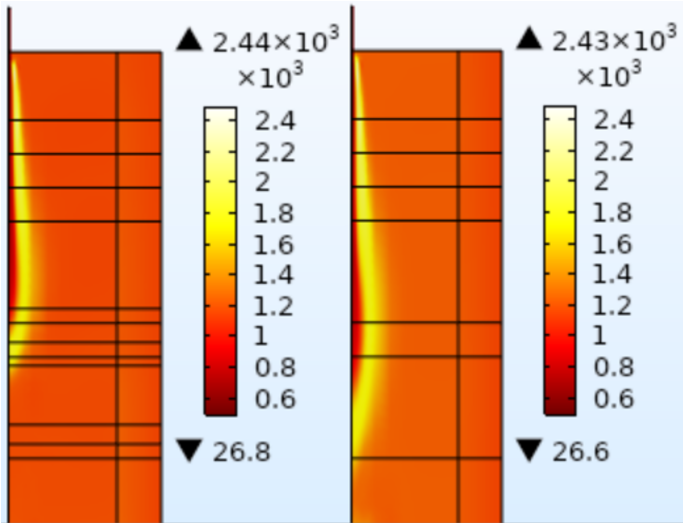

Figure 9. Temperature distribution [°C] at YZ plane of in the furnace with 9 mm fuel pipe diameter and fuel mass flow rate of 0.003 kg/s passing through (a) first burner and the (b) second burner. The high temperature is restricted to a narrow flame outline. The combustion at the first burner occurs readily as compared to the second burner.

needed). The temperatures from both model and the image of the thermograpic camera are extracted at the same plane as shown in Figure 10. The extracted values are documented in Table 8. It can be observed that the values computed from the model compares well with the measured values. The model values in the plane seems to be more uniform as compared to the measured values. Therefore, at one point of location the difference is as less as 0.08% while at another point the difference is around 6.8%.

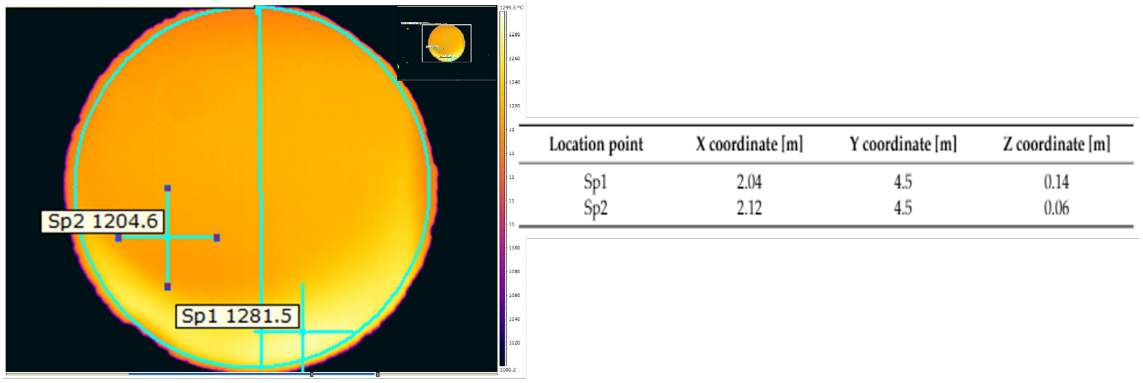

Location point	X coordinate [m]	Y coordinate [m]	Z coordinate [m]
Sp1	2.04	4.5	0.14
Sp2	2.12	4.5	0.06

Figure 10. Location of the temperature computation from (a) measurement from the IR camera and (b) corresponding coordinates of points from the model.

Table 8. Comparison of the temperature values from the model and the measurement using IR camera

Model [degC]	Measurement [degC]	Relative change with respect to the measurement
1208	1204	-0.3%
1209	1281	5.6%

The calculated chemical species values from the test case are compared with the measured values. The volume percentage of chemical species such as O_2 and CO_2 are carried out at several locations in the furnace using Testo 350 flue gas analyser. Figure 11 shows the location at which the measurements are carried out. The volume percentage of chemical species are extracted at the same locations. Table 9 and 10 show the comparison of volume percentage calculated with the test case and the measured values for O_2 and CO_2, respectively. It can be observed that at Points 1, 2, 4 and 6, the values are comparable. While at Point 3 and 6, there are significant differences. The measured values in a particular region are uniform as opposed to the values from the test case model. The uniformity in the measured values shows that the chemical species are diffusing well in reality at particular region. Furthermore, it can be observed that the O_2 concentration at the outlet, i.e. at points 4,5 and 6 is lower compared to the measured data. This difference can be explained with the steady state assumption of the model. In reality, the fuel is injected with pulses while the air injection occurs continuously. Therefore, the CH_4 concentration is higher in the model compared to reality. Therefore, more O_2 is consumed in the model to achieve complete combustion. This leads to lower O_2 concentration at the outlet stream from the model.

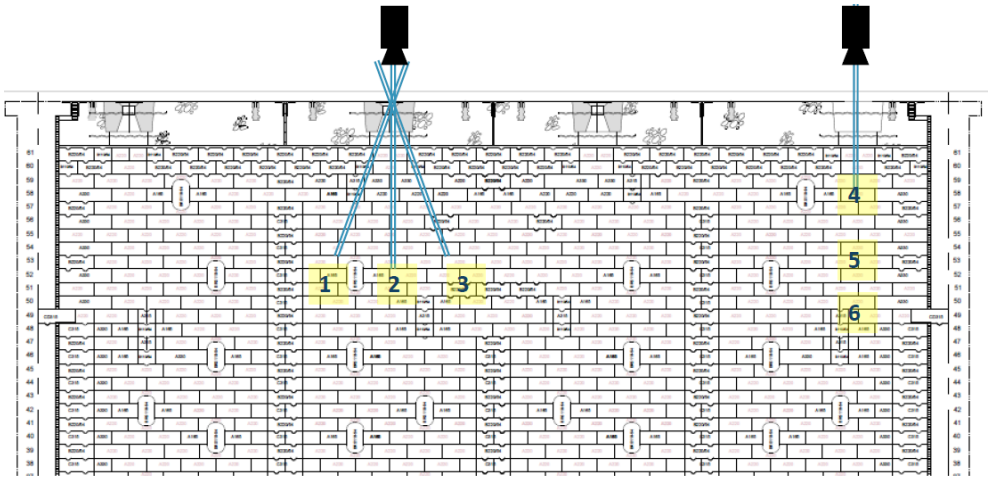

Figure 11. Location of the measurement points in the furnace. Aluchemie measured volume percentage of chemical species at the given locations.

Table 9. Comparison of volume percentage of O_2 calculated by test case model with measurements

O_2	Test case model [vol%]	Measurement average [vol%]	Difference in the values
Point 1	17.9	17.0	0.9
Point 2	16.4	16.5	-0.1
Point 3	5.72	16.0	-10.2
Point 4	9.34	11.0	-1.6
Point 5	0.57	7.00	-6.4
Point 6	6.90	9.00	-2.1

Table 10. Comparison of volume percentage of CO_2 calculated by test case model with measurements

CO_2	Test case model [vol%]	Measurement average [vol%]	Difference in the values
Point 1	0.42	2.00	-1.5
Point 2	1.09	2.00	-0.9
Point 3	5.99	3.00	2.9
Point 4	4.37	6.00	-1.6
Point 5	8.26	8.00	-0.2
Point 6	5.47	6.50	-1.0

4.2. Effect of diffusion on transport of chemical species

The results from the test case model motivates to study the effect of different tuning of the diffusion parameter. The effects of diffusion on the transport of chemical species are studied in this section. The diffusion is varied using a tuning parameter as provided in Equation 11. The diffusion in the transport equation increases as the value of the tuning parameter (δ_{id}) approaches a value of unity. The tuning parameter of zero suggests that no such additional isotropic diffusion is added to the transport of chemical species.

Figure 12 shows the mass fraction of CH_4 for different values of δ_{id}. As can be seen from the figure, the increase in δ_{id} increases the diffusion dominance of the flame. The diffusion parameter also determines the extent of mixing in the furnace. When such additional diffusion is not added (δ_{id}=0), the lesser mixing causes incomplete reaction in the furnace. This results in the small fraction of CH_4 present in the outlet stream. As the values of δ_{id} increase from 0.1 to 0.5, the spreading of the jet near the burner increases while decreasing the length of the jet. In other words, the diffusive nature of the jet is increasing, while the convective dominance of the jet (as observed in the case of δ_{id}=0) is decreasing.

The O_2 component of the air stream reacts with CH_4 as soon as it mixes with the fuel stream. The reaction zone is defined as the region in which mixing occurs. Since the extent of mixing is governed by the diffusion parameters, the effect can be analysed for mass fraction of O_2 and CO_2 as well. Figure 13 and 14 shows the mass fraction of O_2 and CO_2, respectively. It can be seen from Figure 13 that for δ_{id}=0 the lower values of O_2 are restricted to a streamline. This also means that the reaction zone is confined to this region. In other words, the mixing of two streams is limited to a single stream if additional diffusion is not added. With increasing values of δ_{id}, the mixing of the two streams is spread over a larger region allowing reaction to occur in a wider stream. This spread is accompanied with a lowering of the largest value of mass fraction of O_2 with increasing δ_{id} in the domain of computation. This effect can also be visualized from the mass fraction of CO_2 in Figure 14. The appearance of CO_2 is limited in the case of no additional diffusion. While the CO_2 is spread out as we increase the diffusion in the transport equations.

The right choice of δ_{id} is required in order to obtain comparable results with the measurements. As discussed in the earlier section, the volume percentage of chemical species such as O_2 and CO_2 are compared with the measured values at the locations shown in Figure 11. Table 11 and 12 shows the volume percentage of O_2 and CO_2, respectively. The variation of the volume percentage with different values of δ_{id} is compared in these tables. The comparison is carried out by calculating the relative change with respect to the measurement values. The values represented in red color are the values that have less relative change with respect to the measurements for a particular location point. The observation from these tables suggest that the values comparable with measurements are mostly associated with δ_{id}=0.0 and δ_{id}=0.1. Furthermore the root-mean-square deviation is calculated for all the location points for a given value of δ_{id}. The lowest value of the root-mean-square deviation for O_2 is when δ_{id}=0.0. While, the root-mean-square deviation for CO_2 is lowest when δ_{id}=0.1. For O_2, the root-mean-square deviation for δ_{id}=0.1 is slightly higher. Moreover, the measurements suggest that the two chosen regions in the furnace (as shown in Figure 11) do not show a drastic difference

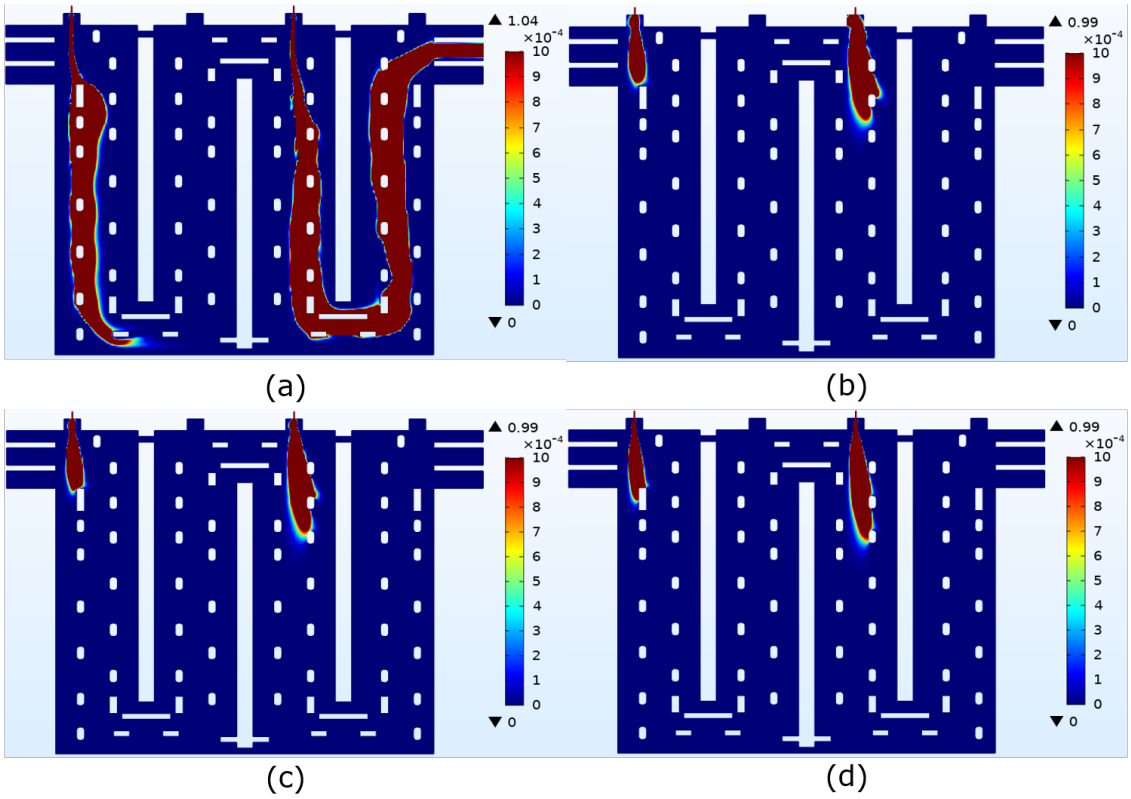

Figure 12. Mass fraction of CH_4 at XY plane (Z=0.27 m) for (a) δ_{id}= 0, (b) δ_{id}= 0.1, (c) δ_{id}= 0.3 and, (d) δ_{id}= 0.5. The diffusion improves as the tuning parameter increases from 0 to 0.5. Higher diffusion leads to increased mixing which results in faster combustion. This implies negligible CH_4 fraction at the outlet streams for higher tuning parameters.

if we vary either the X or Y coordinate. This observation is valid while using additional diffusion. Furthermore, the extent of such diffusion should be limited by a smaller value of δ_{id}. For higher values of δ_{id}, the simulation results vary significantly from the measured values. Therefore, some amount of artificial diffusion is included to obtain a better agreement with the experimental values of O_2 and CO_2 concentrations.

As discussed earlier, the effect of additional diffusion causes more mixing. In this paper, the eddy dissipation model is used for combustion. Therefore, an increase in the mixing of the two streams results in the increase in combustion process. The increase in combustion implies that more reactant is consumed producing more product. This can be validated from the comparisons given in Table 11 and 12. As we increase the value of δ_{id} (thereby increasing diffusion), the value of O_2 decreases. While, there is an increase in the value of CO_2 at a particular location. Moreover, the comparison of the numerical results of mass fraction of O_2 with the measured data show that the mass fraction of O_2 is underestimated with model for all tuning parameters. As explained earlier, this can be attributed to the steady state assumption of the model. In reality, the fuel is injected in pulses and therefore, the model overestimates the fuel input. Consequently, higher O_2 is required for the combustion resulting into lower values of O_2 as compared to measured data. Furthermore, it is difficult to control the fuel injection mass flow rate in the furnace if the pulsating nature is changed to continuous injection through burner. Therefore, the discrepancy in the results of numerical model and the measured data can be explained. Further, the trials on finding effect of artificial diffusion on the temperature and thermal NOx are carried out. The chemical source term R_i defined by Equation 15 and 16, depends non-linearly on the species concentration w_i. Thus, the changes in R_i, temperature and thermal NOx concentration due to changes in w_i and artificial diffusion in the transport equations for w_i are hard to quantify a-priori.

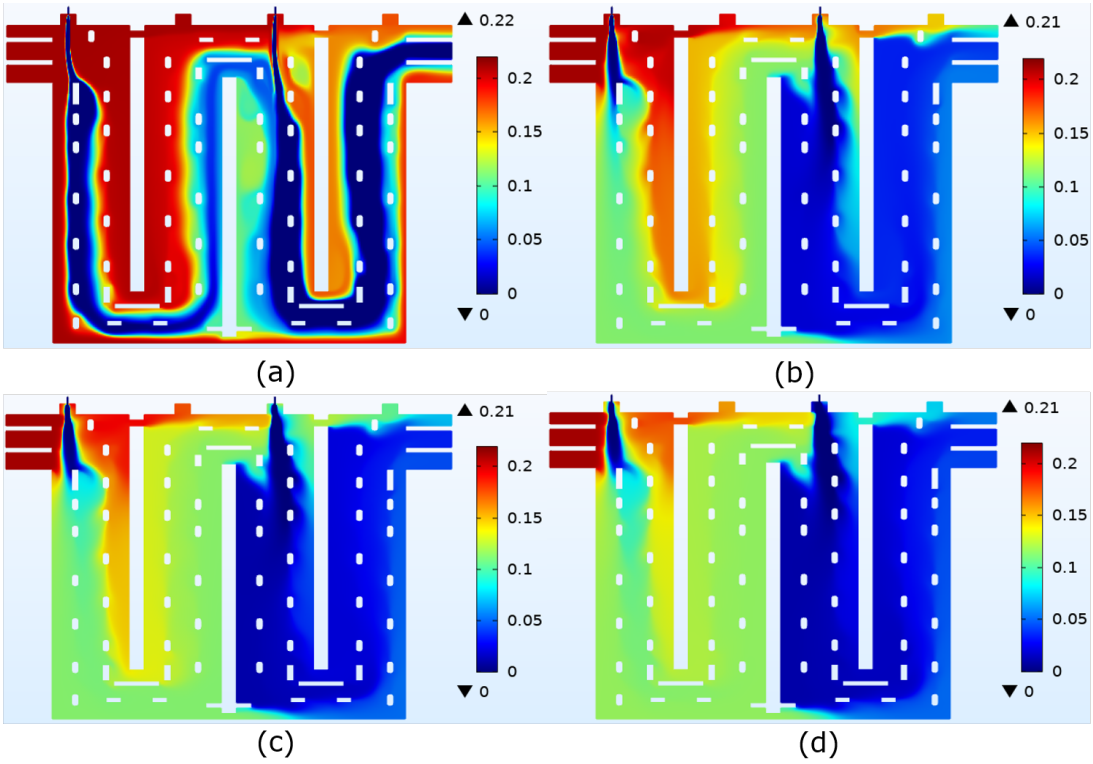

Figure 13. Mass fraction of O_2 at XY plane (Z=0.27 m) for (a) δ_{id}= 0, (b) δ_{id}= 0.1, (c) δ_{id}= 0.3 and, (d) δ_{id}= 0.5. The diffusion improves as the tuning parameter increases from 0 to 0.5. This leads to wider reaction zones with increase in the tuning parameter. Therefore, the lower mass fraction of O_2 at the outlet is not restricted to a narrow stream for higher tuning parameters as observed from measurements.

Table 11. Volume percentage of O_2 for different values of δ_{id} that controls diffusion

O_2	**δ_{id}=0.0 [vol%]**	**δ_{id}=0.1 [vol%]**	**δ_{id}=0.3 [vol%]**	**δ_{id}=0.5 [vol%]**	**Measurement average [vol%]**
Point 1	17.9	13.0	11.4	10.6	17.0
Point 2	16.4	11.4	10.6	10.3	16.5
Point 3	5.72	10.2	10.1	10.2	16.0
Point 4	9.34	3.78	3.39	3.16	11.0
Point 5	0.57	3.58	2.97	2.92	7.00
Point 6	6.90	4.51	3.84	3.68	9.00
Relative change with respect to the measurement					
Point 1	0.05	-0.24	-0.33	-0.38	0.00
Point 2	-0.01	-0.31	-0.36	-0.38	0.00
Point 3	-0.64	-0.36	-0.37	-0.36	0.00
Point 4	-0.15	-0.66	-0.69	-0.71	0.00
Point 5	-0.92	-0.49	-0.58	-0.58	0.00
Point 6	-0.23	-0.50	-0.57	-0.59	0.00
Root mean square deviation					
	5.08	5.15	5.79	6.04	0.00

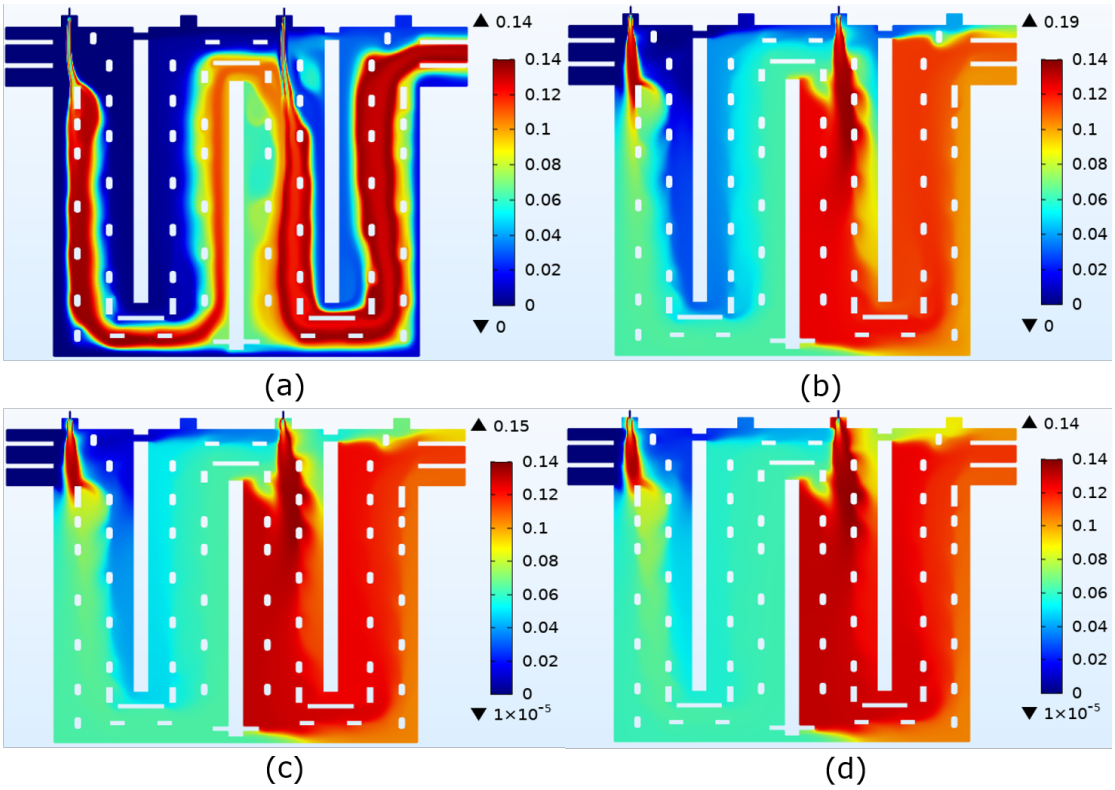

Figure 14. Mass fraction of CO_2 at XY plane (Z=0.27 m) for (a) δ_{id}= 0, (b) δ_{id}= 0.1, (c) δ_{id}= 0.3 and, (d) δ_{id}= 0.5. The diffusion improves as the tuning parameter increases from 0 to 0.5. This leads to wider reaction zones with increase in the tuning parameter. Therefore, the higher mass fraction of CO_2 at the outlet is not restricted to a narrow stream for higher tuning parameters as observed from measurements.

Table 12. Volume percentage of CO_2 for different values of δ_{id} that controls diffusion

CO_2	δ_{id}=0.0 [vol%]	δ_{id}=0.1 [vol%]	δ_{id}=0.3 [vol%]	δ_{id}=0.5 [vol%]	Measurement average [vol%]
Point 1	0.42	2.66	3.38	3.74	2.00
Point 2	1.09	3.42	3.76	3.87	2.00
Point 3	5.99	3.94	4.00	3.94	3.00
Point 4	4.37	6.88	7.06	7.17	6.00
Point 5	8.26	6.98	7.25	7.28	8.00
Point 6	5.47	6.55	6.85	6.93	6.50
Relative change with respect to the measurement					
Point 1	-0.79	0.33	0.69	0.87	0.00
Point 2	-0.46	0.71	0.88	0.94	0.00
Point 3	1.00	0.31	0.33	0.31	0.00
Point 4	-0.27	0.15	0.18	0.20	0.00
Point 5	0.03	-0.13	-0.09	-0.09	0.00
Point 6	-0.16	0.01	0.05	0.07	0.00
Root mean square deviation					
	1.63	0.92	1.14	1.25	0.00

4.3. Effect of variation of fuel velocity

In the earlier section, the variation in the Peclet number is based on the changes in the diffusion coefficient. The decrease in the Peclet number by increasing the diffusion coefficient resulted in

increased mixing of fuel and oxidizer stream. In this section the effect of variation on the fuel jet velocity is studied. Figure 15 shows the mass fraction distribution of CH_4 at the symmetry plane for varying fuel inlet velocities. It can be seen from the figure that for higher velocity, the CH_4 does not readily react with oxidizer in case of 0.0037 kg/s. This can be attributed to the reduced mixing due to higher momentum as well as the increased quantity of fuel. For a fixed diameter of fuel pipe, the increase in velocity also accounts for the increase in the fuel quantity. For a fixed oxidizer concentration, it takes longer to consume all CH_4. Therefore, the length of CH_4 jet increases with increase in the velocity.

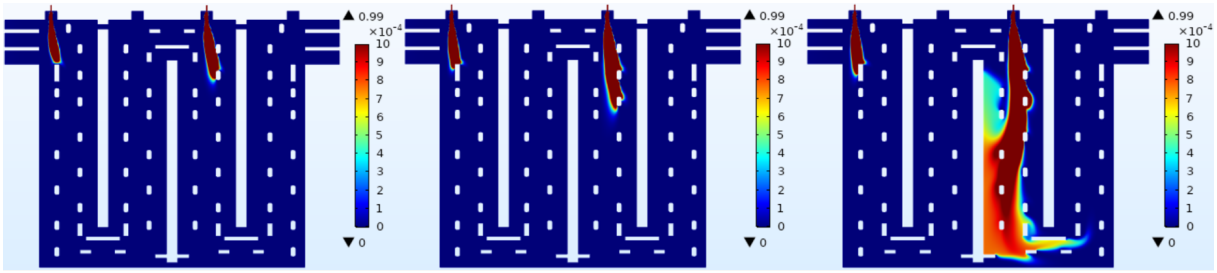

Figure 15. The CH_4 mass fraction distribution at the symmetry plane for varying fuel inlet mass flow rate of (a) 0.002 kg/s (b) 0.003 kg/s and (c) 0.0037 kg/s with 9 mm fuel pipe diameter. The higher mass flow rate results in the higher momentum of the jet as well as higher amount of CH_4 mass fraction. Therefore, the region of unreacted CH_4 is higher with increased mass flow rate.

Figure 16 shows the temperature distribution at the YZ plane cutting through the first burner. As can be seen from the figure, the maximum temperature in the furnace increases with the increase in the velocity of fuel jet. The advection term in the transport equation of the chemical species increases with increase in velocity. In other words, for a given geometry and diffusion rate, the Peclet number increases with increase in the velocity of fuel jet. With this concept, the temperature in the furnace should decrease with the increase in the velocity. However, the increase in the fuel jet also increases the fuel in the furnace. The heating section of the anode baking furnace is always a lean mixture. This means that there is always enough oxidizer for burning. Therefore, the overall combustion in the furnace increases thereby increasing the temperature.

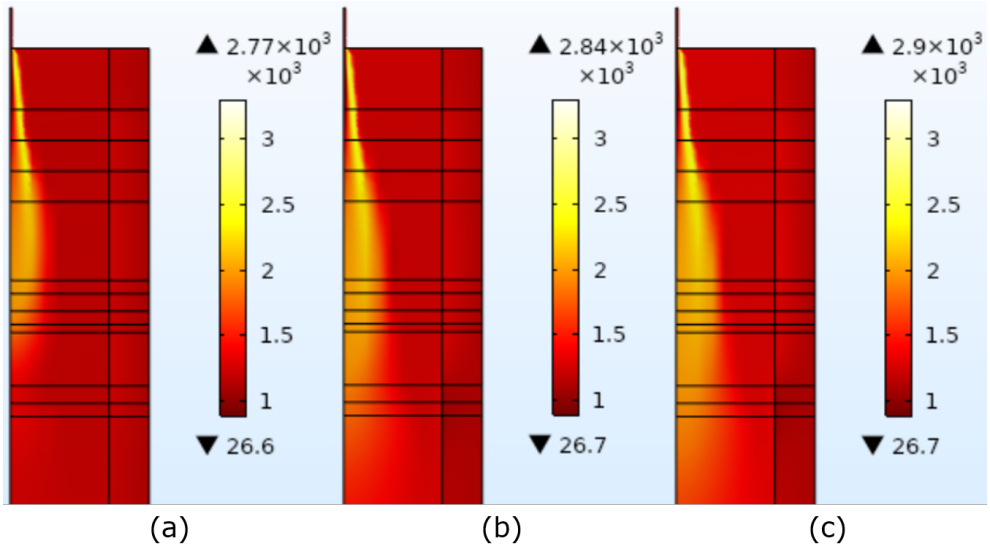

Figure 16. The temperature distribution (in ^{0}C) at the YZ plane through burner 1 for varying fuel inlet mass flow rate of (a) 0.002 kg/s (b) 0.003 kg/s and (c) 0.0037 kg/s with 9 mm fuel pipe diameter. The increased mass flow rate increases the temperature in the furnace due to higher amount of fuel and faster combustion resulting from higher turbulence.

4.4. Effect of increasing the fuel pipe diameter

In the previous section, the increase of velocity resulting into the increase in the amount of fuel in the excess of oxidizer environment is observed. With increasing the velocity, the advection term is also increased. However, in the previous analysis these effects have been suppressed by the predominant effects of increasing the fuel amount. In this section, the effects of advection are studied in such a way that the fuel amount remains the same. This is carried out by increasing the fuel pipe diameter. The diameter of the fuel burner pipe is increased from 9 mm to 13 mm. The velocity of the fuel inlet through the 13 mm fuel pipe is such that the mass flow rate of fuel is equal to that through 9 mm diameter. Earlier in Table 7 the values of velocities for the two fuel pipe diameters that yields equal mass flow rate of fuel injected in the furnace has been listed. The advection term of the flow dynamics with two fuel pipe diameters are different. Moreover, in this comparison the air/fuel ratio for a given mass flow rate of fuel is constant for the two fuel pipe diameters. Therefore, the difference in the results for the two fuel pipe diameters are governed by the difference in the advection.

Figure 17 shows the velocity profile at the symmetry plane for the mass flow rate of 0.003 kg/s with two fuel pipe diameters. The higher momentum of the 9 mm diameter fuel pipe results in a deeper penetration of the jet in the furnace. The difference in the momentum of the two jets further leads to variation in turbulence. This can be quantified by comparing the turbulent viscosity ratio as shown in Figure 18. The comparison shows that the turbulent intensity for the 9 mm diameter is higher, especially in the encircled region below the fuel outlet. Due to the higher turbulence produced by the jet of 9 mm diameter, there is higher mixing of the fuel and oxidizer streams. Therefore, the CH_4 from the fuel jet readily reacts with O_2 from the oxidizer stream.

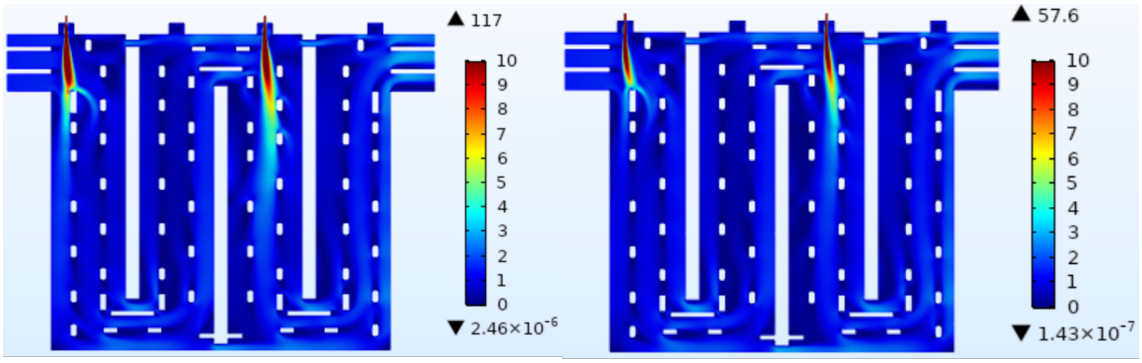

Figure 17. Velocity magnitude [m/s] comparison at the symmetry plane with the fuel pipe diameter of (a) 9 mm and (b) 13 mm for fuel mass flow rate of 0.003 kg/s. The jet is penetrated deeper for 9 mm fuel pipe diameter due to higher momentum.

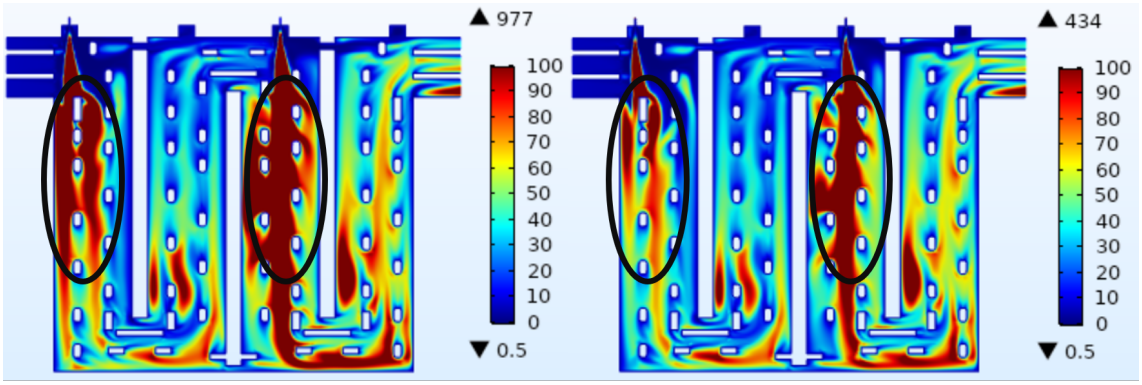

Figure 18. Comparison of turbulent viscosity ratio at the symmetry plane with the fuel pipe diameter of (a) 9 mm and (b) 13 mm for fuel mass flow rate of 0.003 kg/s. Higher turbulence is observed for the 9 mm fuel pipe diameter due to higher velocity magnitude.

Figure 19 shows the mass fraction distribution of CH_4 at the symmetry plane with the two fuel pipe diameters. It can be seen from the comparison that the CH_4 is exhausted by the reaction earlier in case of 9 mm diameter. Whereas, the CH_4 is available till higher depth in case of 13 mm diameter. This aligns with our expectation that due to higher turbulence CH_4 reacts readily with oxidizer in case of 9 mm diameter. This further results in higher temperatures in the furnace for 9 mm fuel pipe diameter. Figures 20 (a) and (b) show the temperature distribution at YZ plane passing through burner 1 for 9 mm and 13 mm diameter fuel pipe, respectively. While, Figures 20 (c) and (d) show the temperature distribution at YZ plane passing through burner 1 for 9 mm and 13 mm diameter fuel pipe, respectively. The maximum temperature with 9 mm fuel diameter pipe is high for both burners 1 and 2 as compared to 13 mm. This is attributed to the higher rate of reaction occurring in accumulated locally in the furnace.

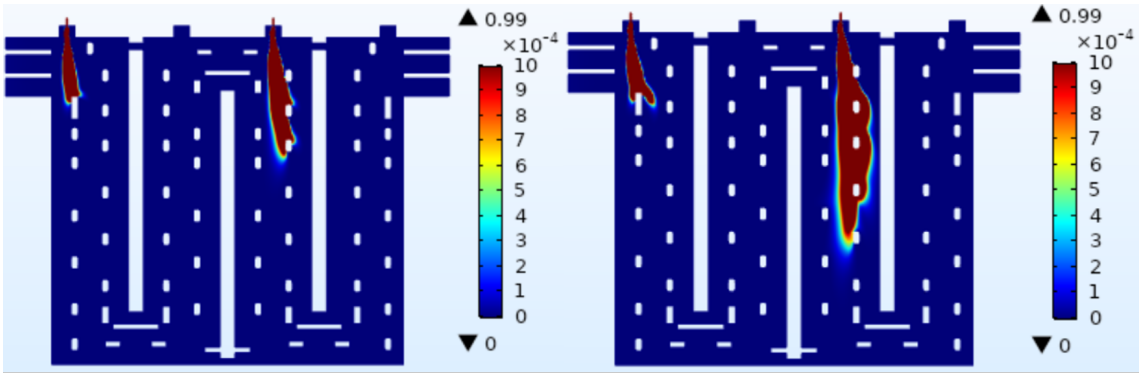

Figure 19. Comparison of mass fraction of CH_4 at the symmetry plane with the fuel pipe diameter of (a) 9 mm and (b) 13 mm for fuel mass flow rate of 0.003 kg/s. With increased diameter, turbulence decreases due to which combustion process is slower resulting into longer unreacted CH_4 jet.

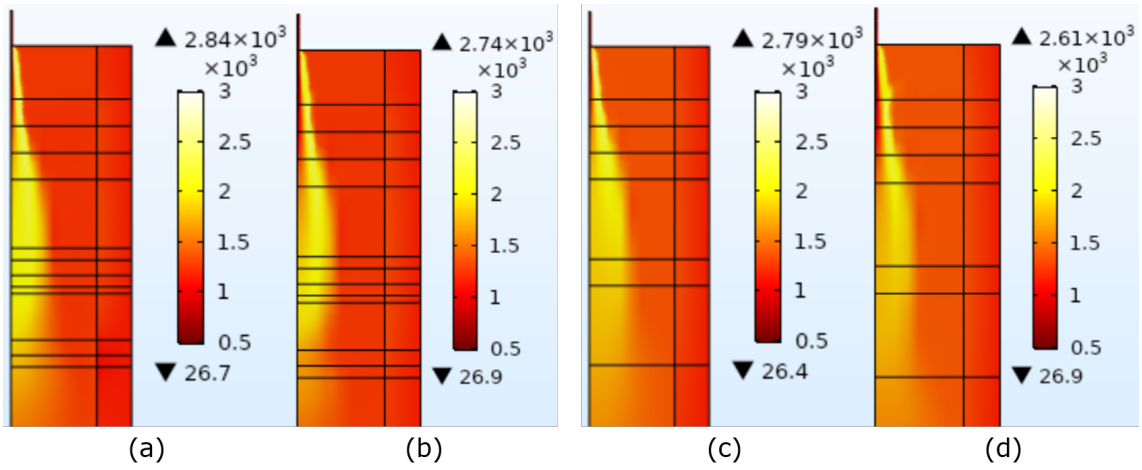

Figure 20. Comparison of temperature [^{o}C] at the YZ plane with the fuel pipe diameter of (a) 9 mm cutting through burner 1 (b) 13 mm cutting through burner 1 (c) 9 mm cutting through burner 2 and (d) 13 mm cutting through burner 2 for fuel mass flow rate of 0.003 kg/s. Due to increased turbulence with 9 mm fuel pipe diameter, combustion is faster and therefore, temperature is higher compared to 13 mm fuel pipe diameter.

5. Impact on NOx due to varying operating conditions

In the above sections, the effect of varying operating conditions on the mass fraction, temperature and turbulent viscosity ratio across the furnace are compared. The thermal NOx in the furnace depends on the temperature, mass fraction of O_2 and mass fraction of N_2. Therefore, the thermal NOx in the furnace can be computed in post-processing with the available results. The Zeldovich mechanism as described in the numerical model equations section is used for calculating the NOx.

Before proceeding into discussion on the calculations of NOx, a summary on the impact of fuel pipe diameter and fuel injection velocity is discussed. Figure 21 shows the temperature at the XY symmetry plane for the studied variations. It can be observed that by increasing the fuel pipe diameter, the maximum temperature in the furnace is lowered. Furthermore, for a particular diameter, increasing velocity of fuel injection increases the temperature. The reason for the increase in the temperature is closely related to the increased turbulence in the furnace. This can be observed from Figure 22 that shows the turbulent viscosity ratio across the furnace at the symmetry XY plane.

Figure 24 shows that the NOx at the XY symmetry plane (Z=0.27 m) for varying velocities and fuel pipe diameters. The comparison of Figure 24 (a) with 24 (b) shows that the overall NOx is higher

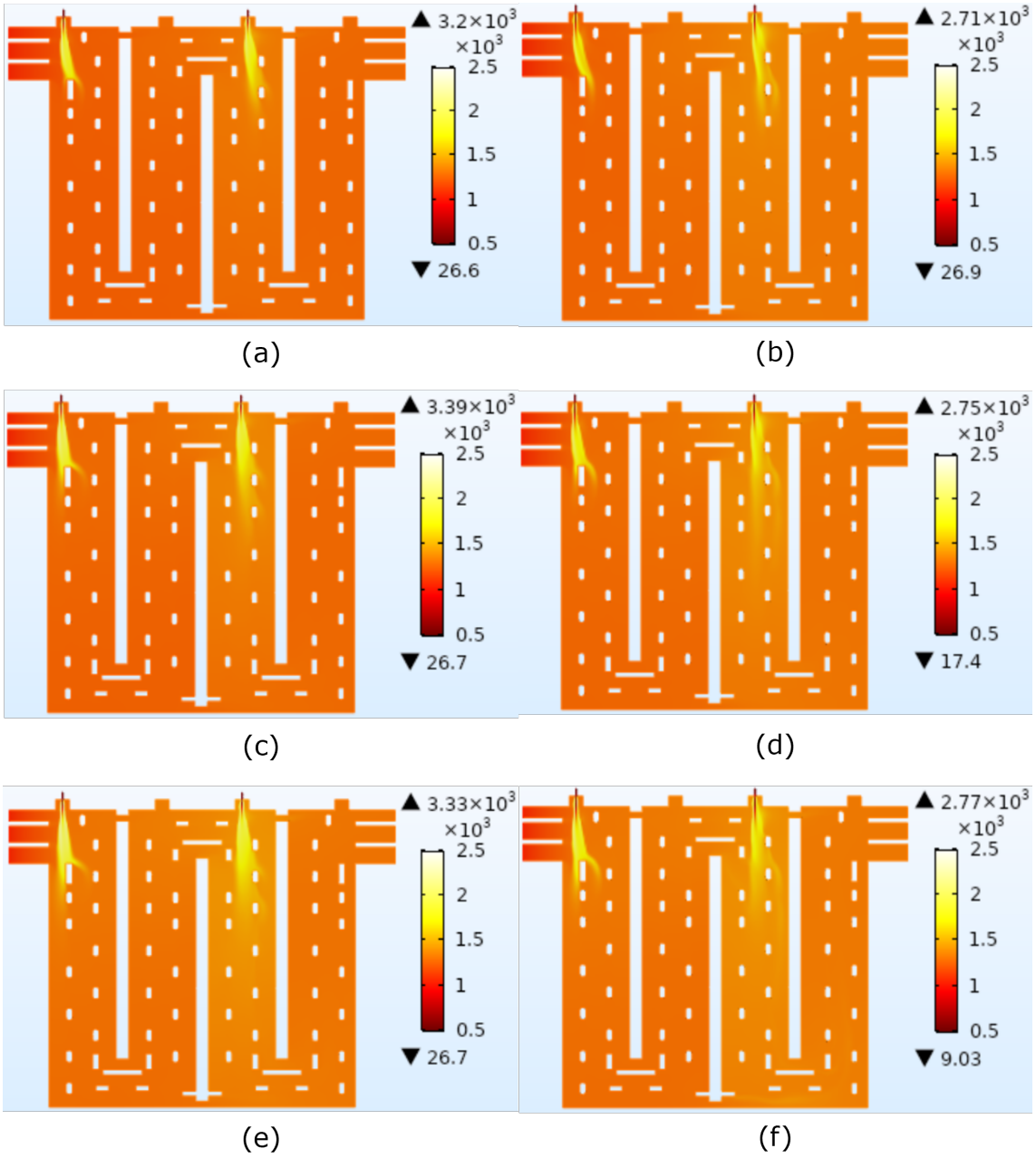

Figure 21. Temperature [^{o}C] at the XY symmetry plane (Z=0.27 m) with varying fuel pipe diameter and mass flow rate of fuel injection (a) 9 mm and 0.002 kg/s (b) 13 mm and 0.002 kg/s (c) 9 mm and 0.003 kg/s (d) 13 mm and 0.003 kg/s (e) 9 mm and 0.0037 kg/s and (f) 13 mm and 0.0037 kg/s. Temperature decreases with increased fuel pipe diameter. It increases with increased mass flow rate of fuel inlet.

in the furnace for the fuel pipe diameter of 9 mm as compared to 13 mm. The same observation can be obtained by comparing Figure 24 (c) with 24 (d) and Figure 24 (e) with 24 (f). The effect of increasing velocity for a particular fuel pipe diameter can also be examined. Comparison of results for 9 mm fuel pipe diameter from Figure 24 (a), (c) and (e) shows that the NOx generation in the furnace increases for increasing value of fuel jet velocity. The similar observation can be obtained by comparing Figure 24 (b), (d) and (f) for 13 mm fuel pipe diameter.

The NOx values are extracted at the same locations represented in Figure 11 where the measurements are carried out. The measurement values are available for the current design with 9 mm fuel pipe diameter and operating conditions with mass flow rate of 0.003 kg/s. These values are

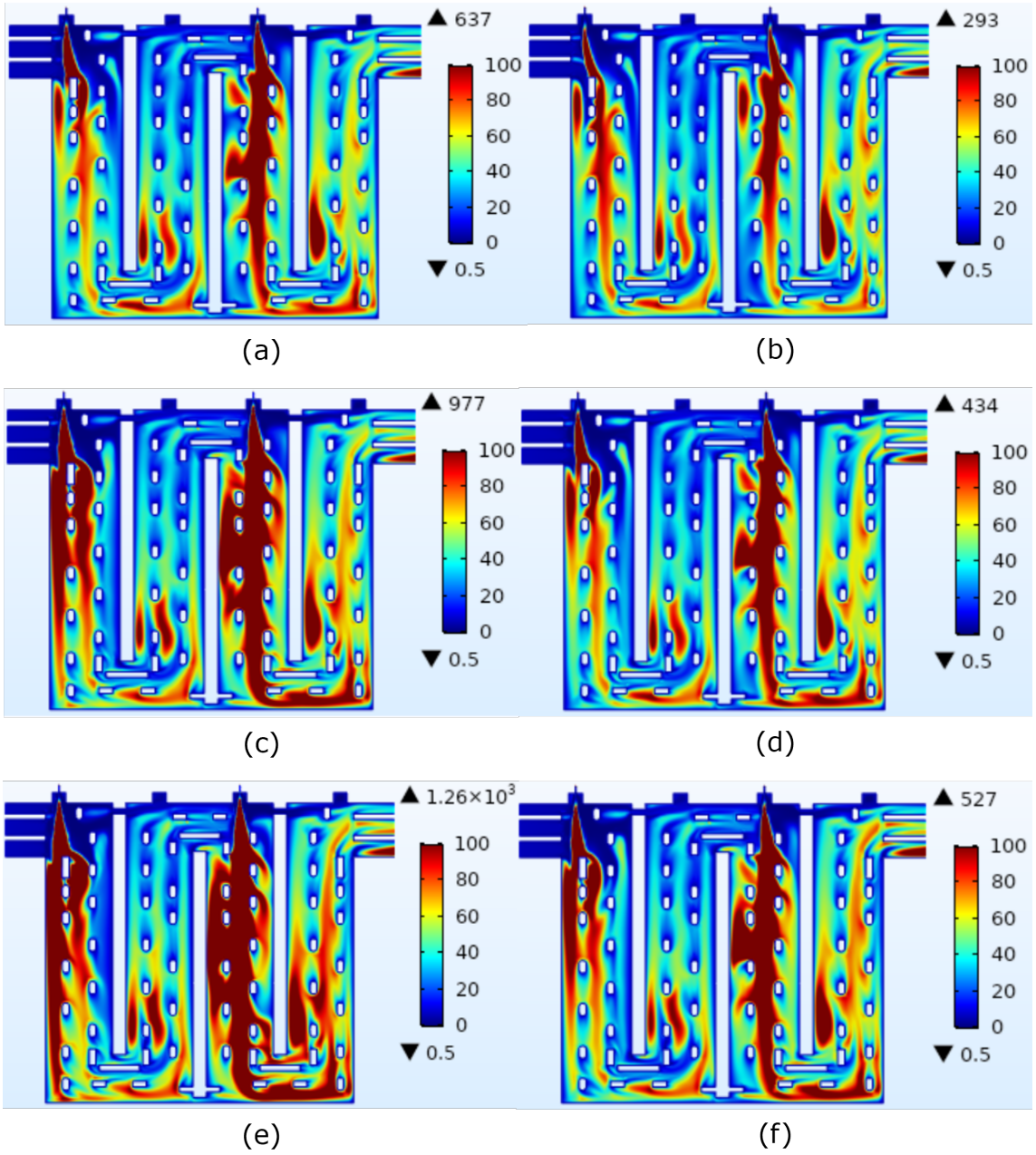

Figure 22. Turbulent viscosity ratio at the XY symmetry plane (Z=0.27 m) with varying fuel pipe diameter and mass flow rate of fuel injection (a) 9 mm and 0.002 kg/s (b) 13 mm and 0.002 kg/s (c) 9 mm and 0.003 kg/s (d) 13 mm and 0.003 kg/s (e) 9 mm and 0.0037 kg/s and (f) 13 mm and 0.0037 kg/s. Turbulent viscosity ratio decreases with decreased fuel pipe diameter. It increases with increased mass flow rate of fuel inlet.

represented by the black plot. The model values are over-predicted as compared to the measured values. As explained earlier, this over-prediction can be attributed to the steady state assumption in the model as opposed to the reality where fuel is injected in a pulsating manner. Due to the steady state assumption, the model over-predicts the injected fuel resulting into higher combustion. This leads to higher temperature in the furnace causing higher NOx. However, with the given results, the trends of NOx can be understood with varying designs and operating conditions. The red and blue colors denote the results of 9 mm and 13 mm diameter fuel pipes, respectively. Moreover, symbols '$\star$', 'o' and '$\triangle$' represent values for mass flow rate of 0.003 kg/s, 0.002 kg/s and 0.0037 kg/s, respectively.

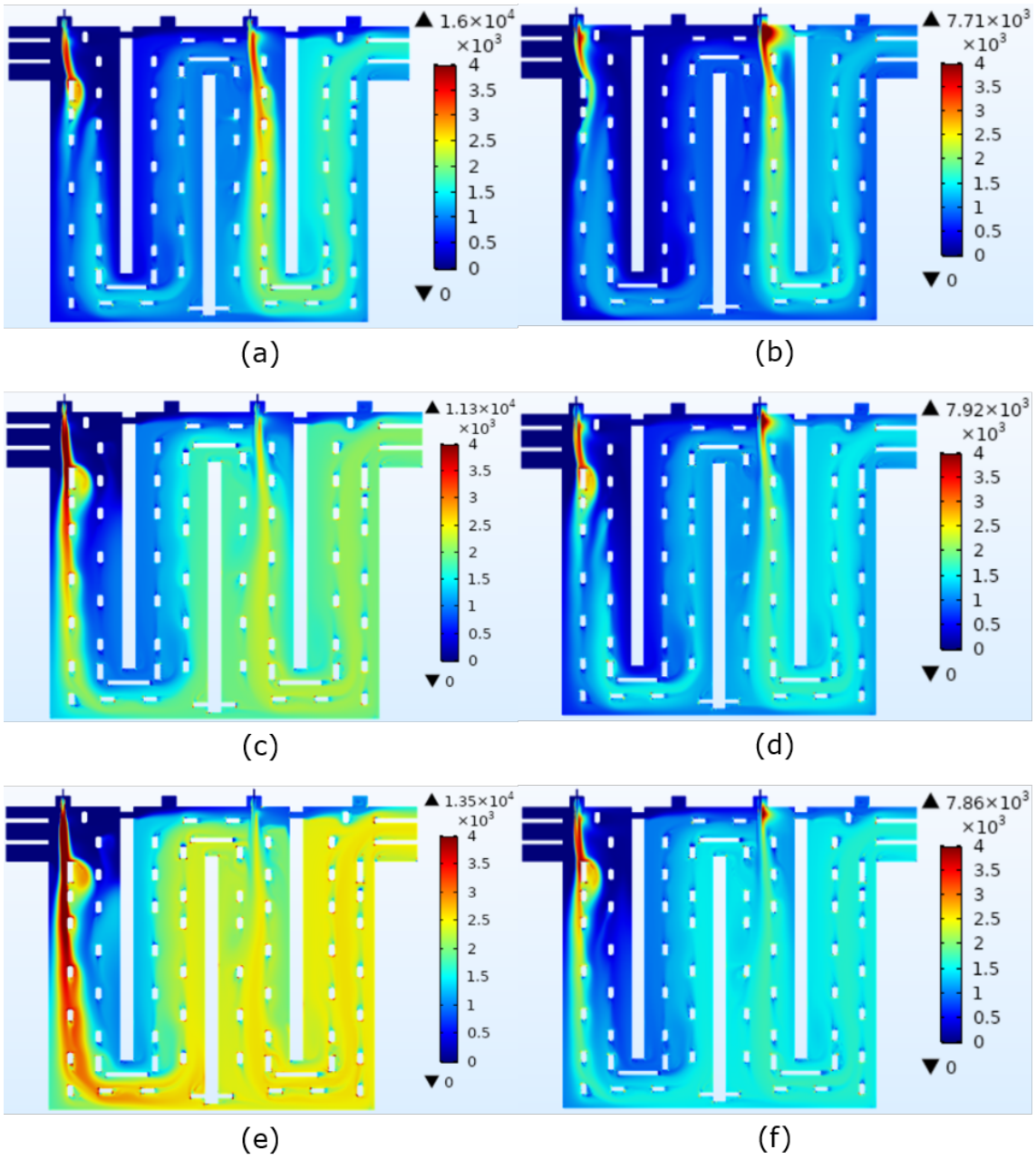

Figure 23. NOx fraction [ppm] at the XY symmetry plane (Z=0.27 m) with varying fuel pipe diameter and mass flow rate of fuel injection (a) 9 mm and 0.002 kg/s (b) 13 mm and 0.002 kg/s (c) 9 mm and 0.003 kg/s (d) 13 mm and 0.003 kg/s (e) 9 mm and 0.0037 kg/s and (f) 13 mm and 0.0037 kg/s. NOx decreases with decreased fuel pipe diameter. While, it increases with increased mass flow rate of fuel inlet.

It can be observed that for a particular symbol, for example '⋆', the red plots are always higher than the blue plots. This suggest that with increase in the fuel pipe diameter, the NOx across the furnace decreases. Furthermore, for a particular color, for example red, the symbol 'o' is always lower than '⋆' which is further lower than '△'. This implies that for a given fuel pipe diameter, the NOx decreases with decrease in the fuel pipe diameter.

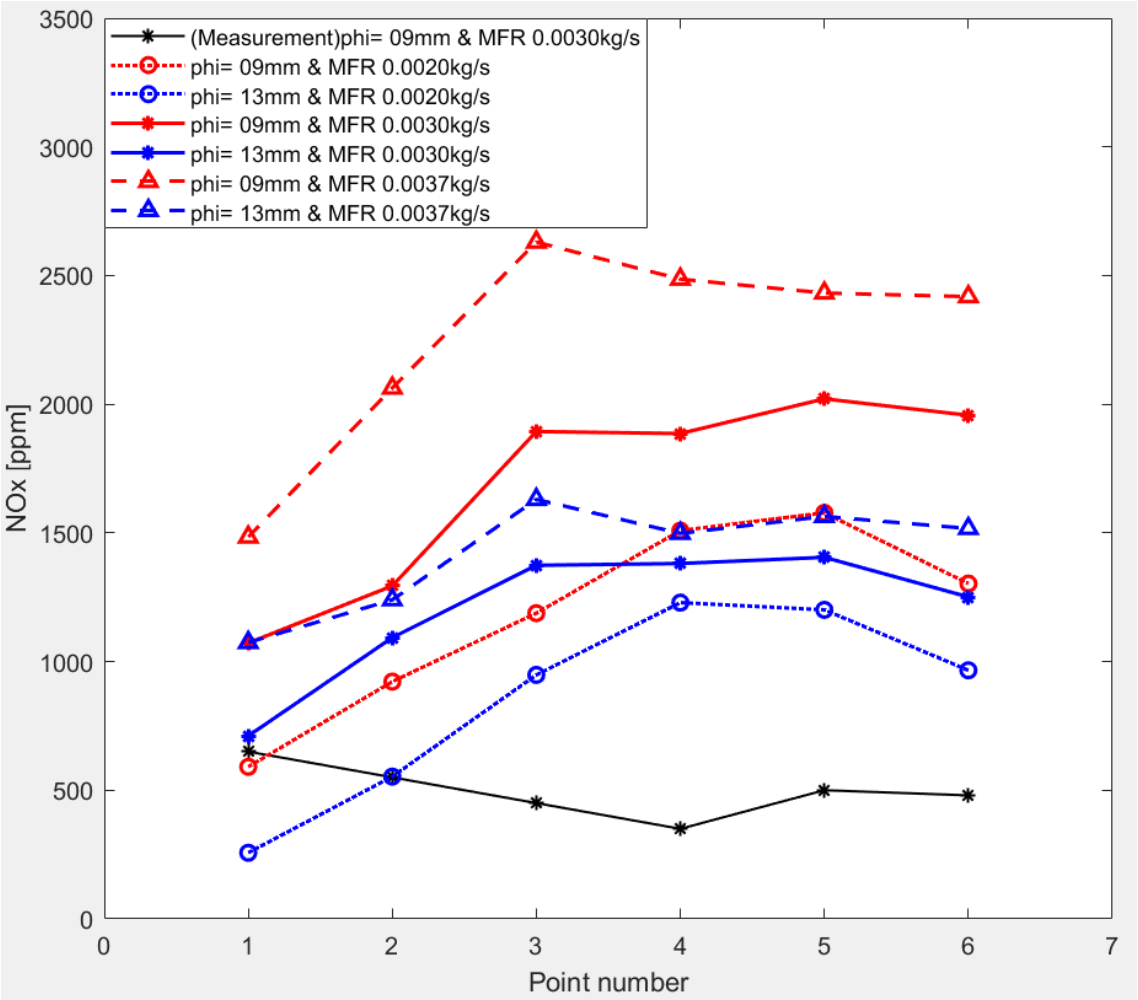

Figure 24. NOx fraction at six measured point locations for varying fuel pipe diameters and fuel injection velocities. Red and blue colors denote the results of 9 mm and 13 mm diameter fuel pipes, respectively. Black color denotes the measured values for 9 mm diameter and 0.003 kg/s. Symbols '$\star$', 'o' and '$\triangle$' represent values for mass flow rate of 0.003 kg/s, 0.002 kg/s and 0.0037 kg/s, respectively. NOx calculated from the model are over predicted as compared to measured values. With increased fuel pipe diameter, NOx decreases for a certain mass flow rate of fuel. While, NOx increases with increase mass flow rate of fuel for a certain fuel pipe diameter.

6. Conclusion

In this paper, a three dimensional model of the heating section of the anode baking furnace is examined to analyse the thermal NOx formation. The COMSOL multi-physics software is used for the modeling of non-premixed turbulent combustion along with the conjugate heat transfer through lining. In the first part of the paper, the calibration of the model is carried out by comparing temperature and species mass fraction with the measured data from Aluchemie. The test model with tuned diffusion parameter that resembles the existing design and operating conditions provide good comparison with the measured data for the temperature. The O_2 mass fraction is underestimated with the model. However, the trend of O_2 mass fraction through the furnace is well predicted.

The fuel mass flow rate and fuel pipe diameter are varied and their effect on the NOx formation are studied. The motivation for the choice of these parameters is based on their effect on the flow dynamics in the furnace. It can be concluded that by decreasing the fuel mass flow rate from 0.0037 kg/s to 0.002 kg/s for the existing fuel pipe diameter of 9 mm, the NOx decreases by 15%. This decrease can be attributed to the decrease in the turbulent viscosity ratio and fuel amount. The

effect of turbulence can further be verified by analysing the variation in the fuel injection velocity by keeping their mass flow rate constant. This is carried out by varying the fuel pipe diameter. It can be inferred that for an existing fuel mass flow rate in the furnace, the increase in the fuel diameter by 45% decreases the NOx formation by 30% in the furnace. This is due to the decreased turbulence viscosity ratio resulting from the decreased velocity of fuel injection. Though the models from this paper overestimates the NOx formation, they serve the purpose of establishing trends of NOx formation. From the overall comparison of six cases with three fuel mass flow rates and two fuel pipe diameters, it can be concluded that by decreasing the fuel mass flow rate and increasing the fuel pipe diameter by 45%, the peak thermal NOx in the furnace decreases by 42%.

References

1. Fluent Ansys. Ansys Fluent Theory Guide. In *ANSYS Inc.*; USA 15317, **2013**; 724-746.
2. Baukal, C.E. Industrial Combustion Pollution and Control. In *Environmental Science & Pollution*; CRC Press: Boca Raton, FL, USA, **2003**; ISBN 9780367578459.
3. Bui, R.T.; Charette, A.; Bourgeois, T. Simulating the process of carbon anode baking used in the aluminum industry. *Metall. Trans. B* **1984**, *15*, 487–492.
4. Peter, S.; Charette, A.; Bui, R. T.; Tomsett, A.; Potocnik, V. An extended two-dimensional mathematical model of vertical ring furnaces. *Metall. Trans. B* **1996**, *27*, 297–304.
5. Zhang, L.; Zheng, C.; Xu, M. Simulating the heat transfer process of horizontal anode baking furnace. *Dev. Chem. Eng. Miner. Process.* **2004**, *12*.
6. Severo, D. S.; Gusberti, V.; Pinto, E. C. V. Adavanced 3D modelling for anode baking furnaces. *Light Met.* **2005**, *697–702*.
7. Oumarou, N.; Kocaefe, D.; Kocaefe, Y.; Morais, B.; Chabot, J. A dynamic process model for simulating horizontal anode baking furnaces. *Mater. Sci. Technol. Conf. Exhib.* **2013**, *3*, 2077.
8. Keller, F.; Disselhorst, J. H. M. Modern Anode Baking Furnace Developments. *Essent. Readings Light Met.* **2013**, 486–491.
9. Tajik, A. R.; Shamim, T.; Zaidani, M.; Abu Al-Rub, R. K. The effects of flue-wall design modifications on combustion and flow characteristics of an aluminum anode baking furnace-CFD modeling. *Appl. Energy* **2018**, *230*, 207–219.
10. Zaidani, M.; Tajik, A. R.; Qureshi, Z.A.; Shamim, T.; Abu Al-Rub, R. K. Investigating the flue-wall deformation effects on performance characteristics of an open-top aluminum anode baking furnace. *Appl. Energy* **2018**, *231*, 1033-1049.
11. Grégoire, F.; Gosselin, L. Comparison of three combustion models for simulating anode baking furnaces. *Int. J. Therm. Sci.* **2018**, *129*, 532–544.
12. Tajik, A. R.; Shamim, T.; Ghoniem, A. F.; Abu Al-Rub, R. K. The Impact of Critical Operational Parameters on the Performance of the Aluminum Anode Baking Furnace. *J. Energy Resour. Technol. Trans. ASME* **2021**, *143*, 1-12.
13. Nakate, P.; Lahaye, D.; Vuik, C.; Talice, M. Analysis of the Aerodynamics in the Heating Section of an Anode Baking Furnace Using Non-Linear Finite Element Simulations. *Fluids* **2021**, *6*, 46.
14. Donea, J.; Huerta, A. *Finite Element Methods for Flow Problems*; John Wiley & Sons: Hoboken, NJ, USA, **1986**.